



Ultrahigh plastic flow in Au nanotubes enabled by surface stress facilitated reconstruction

R. Cao,^a Y. Deng^{b,*} and C. Deng^{c,*}

^aDepartment of Materials Science, Fudan University, 220 Handan Road, Shanghai 200433, China

^bKey Laboratory of Magnetic Resonance in Biological Systems, State Key Laboratory for Magnetic Resonance and Atomic and Molecular Physics, Wuhan Centre for Magnetic Resonance, Wuhan Institute of Physics and Mathematics, Chinese Academy of Sciences, Wuhan 430071, China

^cDepartment of Mechanical Engineering, The University of Manitoba, 15 Gillson Street, Winnipeg MB R3T 5V6, Canada

Received 31 October 2014; revised 25 November 2014; accepted 28 November 2014

Abstract—Metal nanowires are usually strong but are not able to maintain a high plastic flow due to a lack of strain hardening. In this study, we investigated the tensile deformation of a new category of metal nanowires with hollow interiors by atomistic simulations – the so-called metal nanotubes – and revealed that they possess a combination of ultrahigh strength and plastic flow. In particular, it was found that by controlling the wall thickness and axial orientation, ultrahigh plastic flow stress of more than 2 GPa could be maintained at up to ~60% tensile strain in Au nanotubes, whereas the solid Au nanowires of similar size yielded at tensile strain of less than 5%, after which the stress dropped immediately below 1 GPa. Furthermore, a universal trend of surface reconstruction to the energetically favorable close-packed {111} orientation was found in Au nanotubes regardless of the initial orientation, which may be responsible for the unique plasticity in Au nanotubes with extremely thin walls.
© 2014 Acta Materialia Inc. Published by Elsevier Ltd. All rights reserved.

Keywords: Metal nanotubes; Plastic flow; Surface reconstruction; Phase transformation

1. Introduction

Metal nanowires (NWs) have been widely observed to exhibit superior mechanical properties including ultrahigh strength and large elastic limit, mainly due to their high surface-to-volume ratio [1–15]. On the other hand, carbon nanotubes (CNTs) have long been considered the strongest and stiffest materials yet discovered in terms of tensile strength and elastic modulus [16,17]. Inspired by the extraordinary properties of both metal NWs and CNTs, metal nanotubes (NTs) have attracted growing interest in recent years. Approaches based on templating and electrodeposition [18–21] have been developed to grow NTs in various types of metals, e.g. Au [22–25], Ag [26–29], Cu [30]. Additionally, the microstructures of metal NTs can also be well manipulated by controlling the experimental synthesis conditions. For example, both single-crystalline [18,24,29,31,32] and polycrystalline [18,22] metal NTs have been synthesized with the outer diameter varying from less than 1 nm [27] to more than 100 nm [18], and with the wall thickness varying from a few atom layers [25,27] to tens of nanometers [18,24].

Nevertheless, despite the vast effort from both experiments and atomistic simulations that has been devoted to the mechanical characterization of metal NWs and CNTs, only a few investigations via atomistic simulations have been performed on the mechanical characterization of metal NTs [33–42]. Among those studies, Zhang et al. [39] have shown from molecular dynamics (MD) simulations that in metal NTs while the outer surface was in tension as similar to that in metal NWs, either tension or compression could be achieved at the inner surface depending on the wall thickness. In the past, it has been widely reported that the surface stress plays a key role in determining the mechanical properties of metal NWs, especially when the NW diameter is small. For example, it has been found that the surface stress alone can cause a face-centered cubic (fcc) to body-centered tetragonal [43] phase transformation in Au NWs and induce a $\langle 100 \rangle / \{100\}$ to $\langle 110 \rangle / \{111\}$ re-orientation [44] in Cu, Ag and Ni NWs when the NW size is reduced to a few nanometers. Given the complicated stress state of the inner surface and the dramatically increased surface-to-volume ratio in metal NTs, new physics and deformation mechanisms have been observed. For instance, Ji and Park [40] have simulated the tensile deformation of $\langle 100 \rangle / \{100\}$ Cu NTs by MD and found that special non-square NT geometries can bias the reorientation of $\{100\}$ surfaces to lower energy $\{111\}$ surfaces,

* Corresponding authors; e-mail addresses: dengyun@wipm.ac.cn; dengc@ad.umanitoba.ca

which resulted in an unexpected twinning-dominated deformation mode.

Ji and Park [41] have also investigated the elastic deformation of squared Cu NTs under tensile deformation by MD. They found that the yield strength, yield strain and Young's modulus of Cu NTs all strongly depended on the NT orientation and the portion of bulk materials that have been removed. Similar results were confirmed recently by Sun et al. [42] that in cylindrical Au NTs under tensile deformation, the yield stress and Young's modulus of Au NTs could be significantly larger than that in the corresponding solid Au NWs. Su et al. [36] also found that the elastic properties such as the yield strength and Young's modulus in Au NTs strongly depended on the NT axial orientation and the NT wall thickness. However, the atomistic details of the free surface were not discussed in these studies, which should significantly influence the NT structure and the yielding process, especially when the NT wall thickness was reduced to a few atom layers; the ultrathin metal NTs may transform to a dramatically different structure from their bulk form based on previous experiments [25,27] and first principles computations [28] on metal NWs. What is more, no investigation on the plastic deformation of metal NTs has been performed so far.

The aim of this work is to systematically investigate the influences of surface stress on the structural transformation and plastic deformation of single-crystalline Au NTs under uniaxial tensile deformation through MD simulations. Particularly, the influences of NT diameter, wall thicknesses, NT orientation and system temperature will be evaluated in detail.

2. Methodology

In this study, all MD simulations were performed using LAMMPS [45]. The interatomic forces were characterized by embedded-atom-method (EAM) potentials for Au [46]. This potential can accurately reproduce important properties of Au, such as stacking fault energy and twinning fault energy [47], which are key parameters to predict the yielding and plastic deformation in Au under mechanical loading. Cylindrical Au NTs oriented along different directions, including [100], [110] and [111], were created with fixed length of ~ 50 nm. As shown in the schematic of Fig. 1, the outer radius, inner radius and the wall thickness of a NT were defined as R , r and t , respectively. A periodic boundary condition was imposed along the NT axis (z direction), while the NT was kept free in other directions. The simulation time step was set to be 5 fs, to be more efficient while still producing almost the same result as when a timestep of 1 fs was used. Each model was thermally relaxed at temperatures ranging from 10 K to 800 K for 250 ps under zero pressure under isothermal-isobaric ensemble (NPT) prior to the tensile deformation, which was performed at a constant strain rate of 10^8 s^{-1} with canonical ensemble (NVT) following the thermal relaxation. The tensile stress was calculated by adding the local Virial atomic stress [48] along the loading direction over all atoms and dividing by the deformed NT volume. AtomEye [49] was used to visualize the atomistic configurations.

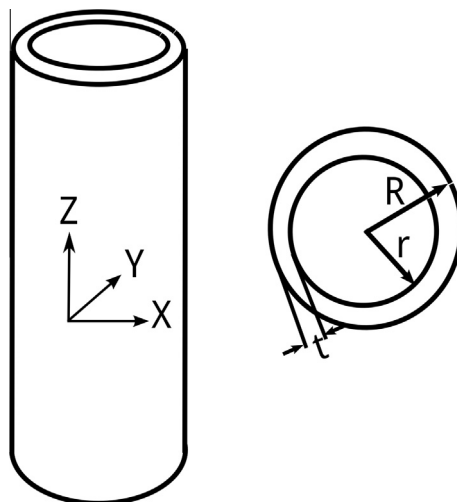


Fig. 1. The schematic of Au NT with R , r and t representing the NT outer radius, inner radius and wall thickness, respectively.

3. Results

3.1. Stress–strain responses in Au NTs

Fig. 2a–c shows the representative tensile stress–strain curves of Au NTs oriented along [100], [110] and [111], respectively, at $T = 300$ K with different combinations of outer radius (R) and wall thickness (t). Solid NWs oriented along each direction were also simulated for comparison. Size-dependent yielding was first noticed, which was similar to that reported by Sun et al. [42]. Furthermore, there was a dramatic transition from sharp yielding (e.g. the stress dropped sharply beyond the yield point) with low plastic flow in solid NWs and NTs with relatively large wall thickness, e.g. $t \geq 2$ nm when $R = 5$ nm, to a smooth yielding with pronounced plastic flow when the NT wall thickness was reduced to 1 nm in all Au NTs. In particular, simulations in Au NTs to the fracture point showed that extraordinarily high flow stress of more than 2 GPa was maintained in both [110] and [100] oriented Au NTs up to the tensile strain of more than 60% when the NT wall thickness was significantly reduced; examples were shown in the insets of Fig. 2a and b, respectively, for [110] and [100] Au NTs with $R = 15$ nm and $t = 1$ nm.

It is worth mentioning that instead of “adding” various types of defects and microstructures such as coherent twin boundaries (CTBs) into the metal NWs in order to achieve high plastic flow [47,48], the results in Fig. 2 indicated that ultrahigh plastic flow can be enabled in metal NWs without sacrificing the yield strength by “subtracting” a significant fraction of volume as an alternative approach. Besides the dramatic difference in plastic flow, it is also important to note the remarkable change in Young's modulus between Au NTs with different wall thickness. For example, the Young's modulus of [100]-oriented Au NTs with $R = 5$ nm increased by $\sim 50\%$ when the NT wall thickness changed from $t = 2$ nm to $t = 1$ nm. In contrast, the Young's modulus of [111]-oriented Au NTs with $R = 5$ nm decreased by more than 60% when the NT wall thickness changed from $t = 2$ nm to $t = 1$ nm. The dramatic change in Young's modulus is a strong indication of

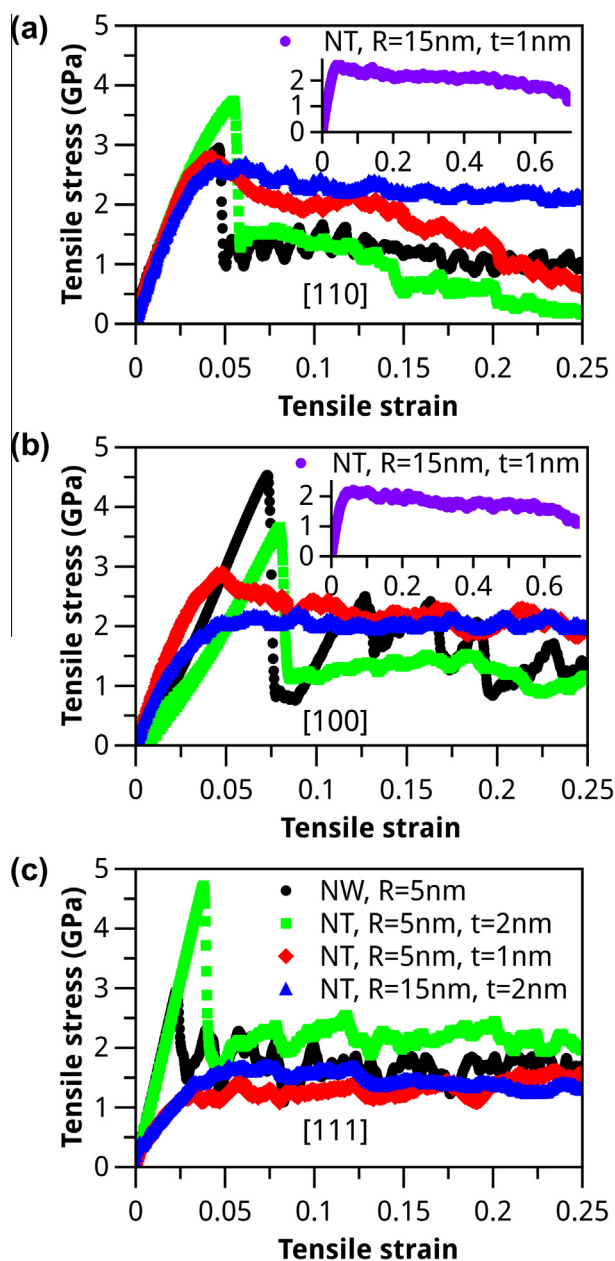


Fig. 2. Tensile stress–strain curves of (a) [110], (b) [100] and (c) [111] Au NTs at $T = 300 \text{ K}$. The insets of (a) and (b) show the stress–strain responses of Au NT with $R = 15 \text{ nm}$, $t = 1 \text{ nm}$ oriented along [110] and [100] during longer simulation time. The symbols (black circle, green square and red diamond) have the same meaning in (a)–(c). (For interpretation of the references to colour in this figure legend, the reader is referred to the web version of this article.)

structural transformation in those Au NTs, which might be the cause of the unusual plastic flow found in Au NTs with extremely thin walls.

3.2. Morphology change and surface reconstruction in Au NTs

Fig. 3 shows the atomistic configuration of [110]-oriented Au NT with $R = 5 \text{ nm}$, $t = 1 \text{ nm}$ after relaxation at 300 K with the cross-section and selected area of the free surface shown in zoomed view. It was found that the free

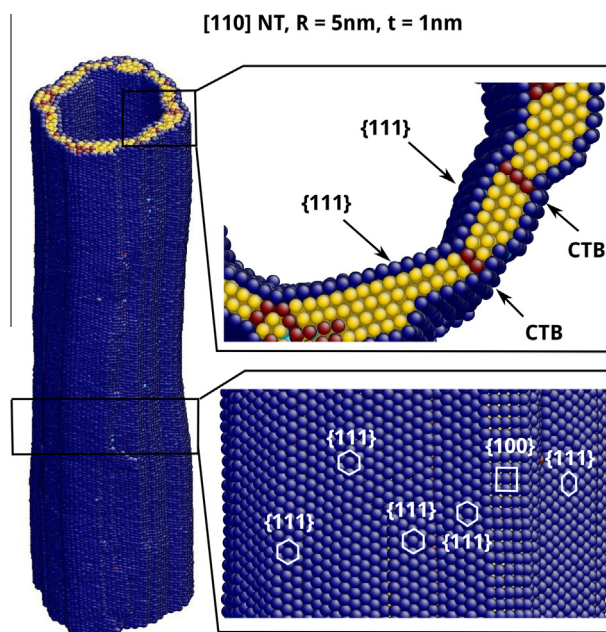


Fig. 3. The atomistic configuration of [110] Au NT with $R = 5 \text{ nm}$ and $t = 1 \text{ nm}$ at 300 K after relaxation. The black arrows indicate the position of CTBs and the formation of {111} surface facets. The white hexagons and square represent the {111} and {100} packing, respectively. The atom colors correspond to the local lattice structures. (For interpretation of the references to colour in this figure legend, the reader is referred to the web version of this article.)

surface was reconstructed to the more energetically favorable {111} facets after relaxation, which was accompanied by the formation of a high density of stacking faults and CTBs (as indicated by the black arrows). It is important to note that the stacking faults and CTBs are all parallel to the NT axis ([110]). Due to the severe morphological change, the dominant mode of plasticity changed accordingly as the NT wall was reduced to $t = 1 \text{ nm}$. Specifically, it was found that the plasticity in Au NW and NTs with large wall thickness (e.g. $R = 5 \text{ nm}$, $t \geq 2 \text{ nm}$) was dominated by CTB-mediated [110] to [100] re-orientation, which is consistent with previous studies from both MD simulations [44] and in situ experiments [50,51]. In contrast, in Au NT with $t = 1 \text{ nm}$ the propagation of newly nucleated partial dislocations and CTBs during plasticity were easily blocked and arrested by the high density of pre-formed stacking faults and CTBs (Fig. 3), resulting in the high plastic flow observed in Fig. 2a.

Although the Au NTs shown in Fig. 3 have a different cross-sectional geometry (circular) and orientation ([110]) as compared to various [100] oriented metal NWs and NTs with square and rhombic cross-sections studied in past MD simulations [43,44,40] and experiments [50,51], it is interesting to find that the reconstruction of free surface towards the close-packed {111} structure seems to be general. In the following, the atomistic configurations of relaxed [100]- and [111]-oriented Au NTs were also examined to validate if similar surface reconstruction has occurred.

Fig. 4a shows the structure of Au NTs initially oriented along [100] with $R = 5 \text{ nm}$, $t = 1 \text{ nm}$ and $t = 2 \text{ nm}$, respectively, after being relaxed at $T = 300 \text{ K}$. While the Au NT with $t = 2 \text{ nm}$ remained almost unchanged after the relaxation, the length and morphology of the Au NT with

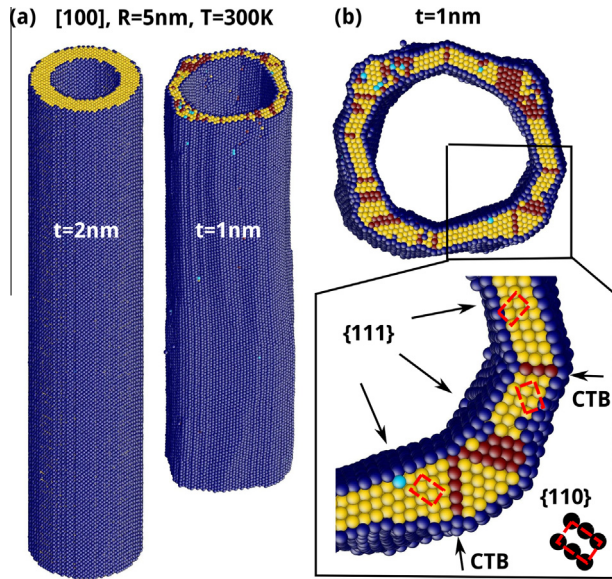


Fig. 4. The atomistic configuration of (a) [100] Au NT with $R = 5$ nm, $t = 1$ nm and $t = 2$ nm at 300 K after relaxation, respectively and (b) the cross-section of [100] Au NT with $R = 5$ nm, $t = 1$ nm. The black arrows indicate the position of CTBs and the formation of {111} surface facets. The red rectangles represent the {110} packing. The atom colors correspond to the local lattice structures. (For interpretation of the references to colour in this figure legend, the reader is referred to the web version of this article.)

$t = 1$ nm has significantly changed. Specifically, the length of the Au NT with $t = 1$ nm reduced from $L_0 \approx 51$ nm (unrelaxed) to $L_R \approx 36$ nm (relaxed), with the ratio $L_R/L_0 = 0.706$, which corresponded to an $\langle 100 \rangle$ to $\langle 110 \rangle$ reorientation in the Au NT; the red dashed rectangles in the zoomed view of Fig. 4b identified the new NT axis to be oriented along $\langle 110 \rangle$. While square $\langle 100 \rangle/\{100\}$ NWs have been widely observed to reorient to $\langle 110 \rangle/\langle 111 \rangle$ under either applied stress or high temperature [44,50,51], it is interesting to find out that circular $\langle 100 \rangle$ Au NTs can reorient to the $\langle 110 \rangle$ direction by surface stress alone. In addition, Fig. 4b shows that the relaxed NT free surface also reconstructed to close-packed {111} facets, during which a high density of CTBs and stacking faults was also formed as similar to the observations in Fig. 3.

The atomistic configuration of relaxed [111]-oriented Au NTs with $R = 5$ nm, $t = 2$ nm and $t = 1$ nm at $T = 300$ K is shown in Fig. 5. As similar to the [100]-oriented Au NTs, an obvious contraction of the [111]-oriented Au NT with $R = 5$ nm, $t = 1$ nm from $L_0 \approx 52$ nm (unrelaxed) to $L_R \approx 35$ nm (relaxed) was observed with the ratio $L_R/L_0 = 0.67$ (Fig. 5a). However, the significant contraction cannot be correlated to a clear reorientation as in [100]-oriented Au NTs.

Nonetheless, a substantial structural transformation also occurred in the [111]-oriented Au NT with $R = 5$ nm, $t = 1$ nm as indicated by the large density of defects formed during the relaxation (Fig. 5b). By carefully examining the morphology of the relaxed Au NT with $R = 5$ nm, $t = 1$ nm (Fig. 5a), it was found that the Au NT tended to form a helical structure; the zoomed view in Fig. 5c indicates that the NT free surface also reconstructed to the energetically favorable {111} facets. The

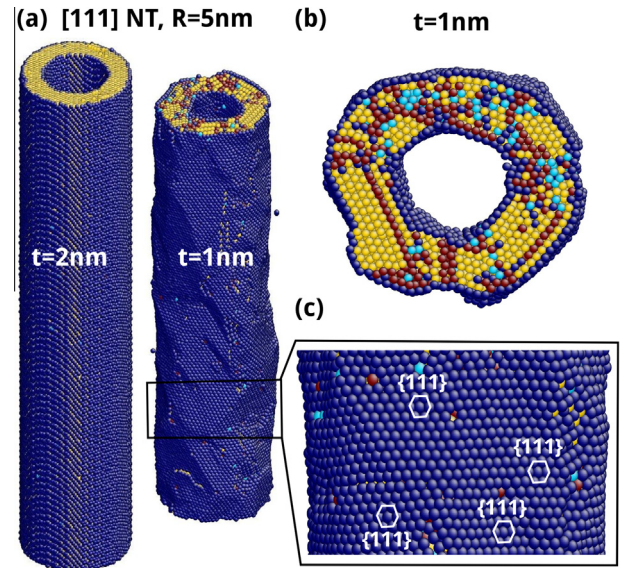


Fig. 5. The atomistic configuration of (a) [111] Au NT with $R = 5$ nm, $t = 1$ nm and $t = 2$ nm at 300 K after relaxation, respectively, (b) the cross-section and (c) zoomed view of selected area on the free surface of [111] Au NT with $R = 5$ nm, $t = 1$ nm. The white hexagons in (c) represent the {111} packing. The atom colors correspond to the local lattice structures. (For interpretation of the references to colour in this figure legend, the reader is referred to the web version of this article.)

morphological change in this particular Au NT could be the cause of the dramatic change in Young's modulus, as found in Fig. 2.

4. Discussion

4.1. Morphology change and surface reconstruction in Au NWs

It has been reported based on first principles studies that as the radius changed, Au tended to form helical ($R \leq 0.3$ nm), multiwalled cylindrical ($R = 0.5 - 1.1$ nm) and fcc-like crystalline structures ($R > 1.1$ nm), respectively [52]. In particular, the multiwalled structures can be viewed as coaxial tubes formed by the helical atomic rows coiling around the wire axis [52]. Since the structure of Au NT with $R = 5$ nm, $t = 1$ nm was not studied in the previous studies, a solid [111] Au NW with $R = 1$ nm was constructed and relaxed at different temperatures from $T = 300$ K to 800 K to validate if the predicted helical structure with close-packed {111} free surface (Fig. 5) was physical. It was found that at both 500 K and 800 K the Au NW would gradually relax to a helical multiwalled structure. Representative snapshots in Fig. 6a show the transformation process at $T = 500$ K, whereas Fig. 6b and c shows the atomistic details of the cross-section and the close-packed {111} free surface with a special helical coiling of atom rows around the wire axis. The structure shown in Fig. 6c is consistent with Au NWs of the same size (e.g. $R = 0.5 - 1.1$ nm) predicted from first principles studies [52]. This is strong indication that the EAM potential of Au [46] used in this study can be used to produce results that are in line with more accurate first principles studies, and the transformations in Au NTs shown in Figs. 3–5 were physical.

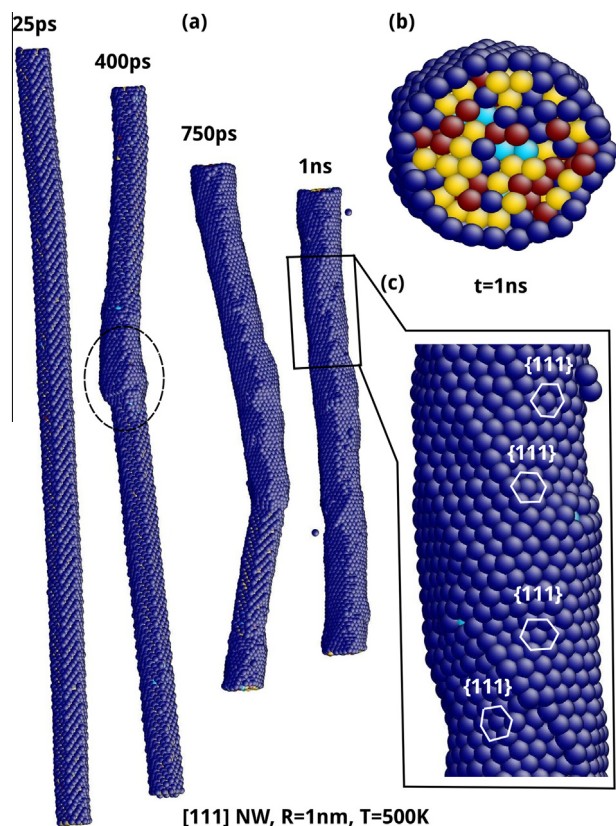


Fig. 6. (a) Snapshots showing the transformation in solid [111] Au NW with $R = 1$ nm during thermal relaxation at $T = 500$ K. The atomistic configuration of (b) the cross-section and (c) selected area of the Au NW after being relaxed at 500 K for 1 ns. The atom colors correspond to the local lattice structure. (For interpretation of the references to colour in this figure legend, the reader is referred to the web version of this article.)

4.2. Influences of temperature and loading mode

Since general phase transformations in materials can be induced by both temperature and stress (e.g. the transformation between $\langle 100 \rangle / \{100\}$ and $\langle 110 \rangle / \{111\}$ orientations in fcc metal NWs [44]), it is important to investigate the influences of temperature and stress on the structural transformations in Au NTs. Overall it was found that the structural transformation in all Au NTs occurred more easily when the temperature was increased; one example is shown in Fig. 7 to demonstrate the temperature induced $\langle 100 \rangle$ to $\langle 110 \rangle$ reorientation in Au NT with $R = 15$ nm, $t = 2$ nm. It can be seen from both the stress-strain curves in Fig. 7a and the atomistic configurations in Fig. 7b that at low temperatures ($T \leq 200$ K), the Au NT remained at $\langle 100 \rangle$ orientation, whereas at high temperatures ($T > 300$ K), the Au NT re-oriented along $\langle 110 \rangle$.

On the other hand, while CTB-mediated $\langle 110 \rangle$ to $\langle 100 \rangle$ reorientation has been found in Au NTs during tension, it is shown in Fig. 8b that the reverse process of CTB-mediated $\langle 100 \rangle$ to $\langle 110 \rangle$ reorientation is also possible in Au NT during compression. The compressive stress-strain curves in Fig. 8a further indicate that the transformation became easier as the wall thickness decreased. It is particularly interesting to find out that in Au NT of $R = 5$ nm and

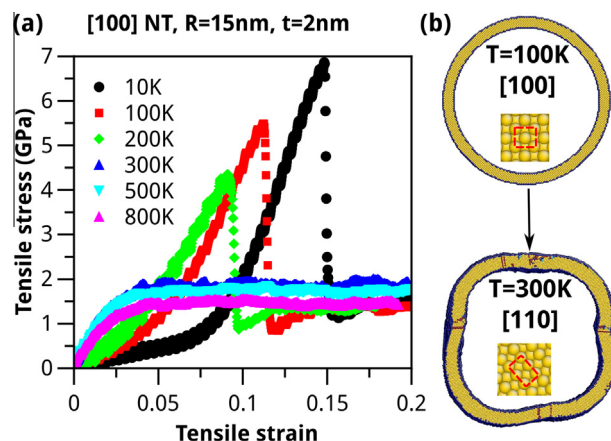


Fig. 7. (a) Tensile stress-strain curves of [100] Au NT with $R = 15$ nm, $t = 2$ nm at various temperatures. (b) The atomistic configuration of the cross-section of the Au NT showing the $\langle 100 \rangle$ to $\langle 110 \rangle$ reorientation when the temperature changed from $T = 100$ K to 300 K. The red dashed square and rectangle in (b) represent $\{100\}$ and $\{110\}$ packing, respectively. The atom colors in (b) correspond to the local lattice structure. (For interpretation of the references to colour in this figure legend, the reader is referred to the web version of this article.)

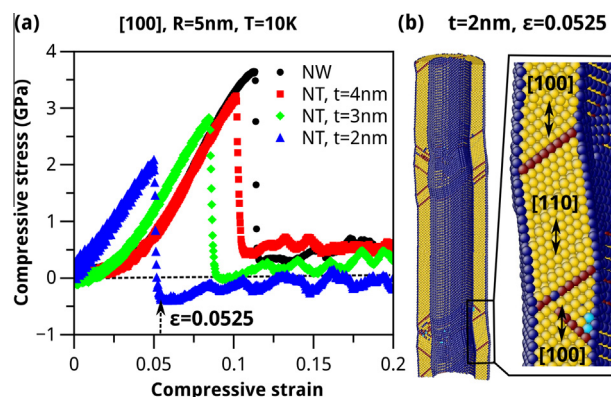


Fig. 8. (a) Compressive stress-strain curves in [100] Au NW and NTs at $T = 10$ K. (b) Representative atomistic configuration showing the CTB-mediated $\langle 100 \rangle$ to $\langle 110 \rangle$ reorientation in Au NT with $R = 5$ nm, $t = 2$ nm. The atom colors in (b) correspond to the local lattice structures. (For interpretation of the references to colour in this figure legend, the reader is referred to the web version of this article.)

$t = 2$ nm the overall stress changed from compressive to tensile (below the dashed line) beyond the yield point and the subsequent $\langle 100 \rangle$ to $\langle 110 \rangle$ transformation became spontaneous. In contrast, external compressive stress was still needed during the subsequent compression of the solid Au NW and Au NT with thick wall (e.g. $R = 5$ nm, $t = 4$ nm) after reaching the yield point (Fig. 8a).

4.3. Fracture of Au NTs

Since the surface stress in $\langle 100 \rangle$ NTs can facilitate the reorientation from $\langle 100 \rangle$ to $\langle 110 \rangle$ and make the compressive deformation easier in $\langle 100 \rangle$ Au NTs than solid NWs, it is reasonable to suspect that the surface stress would make the tensile deformation of $\langle 100 \rangle$ Au NTs more difficult than solid Au NWs. In other words, the

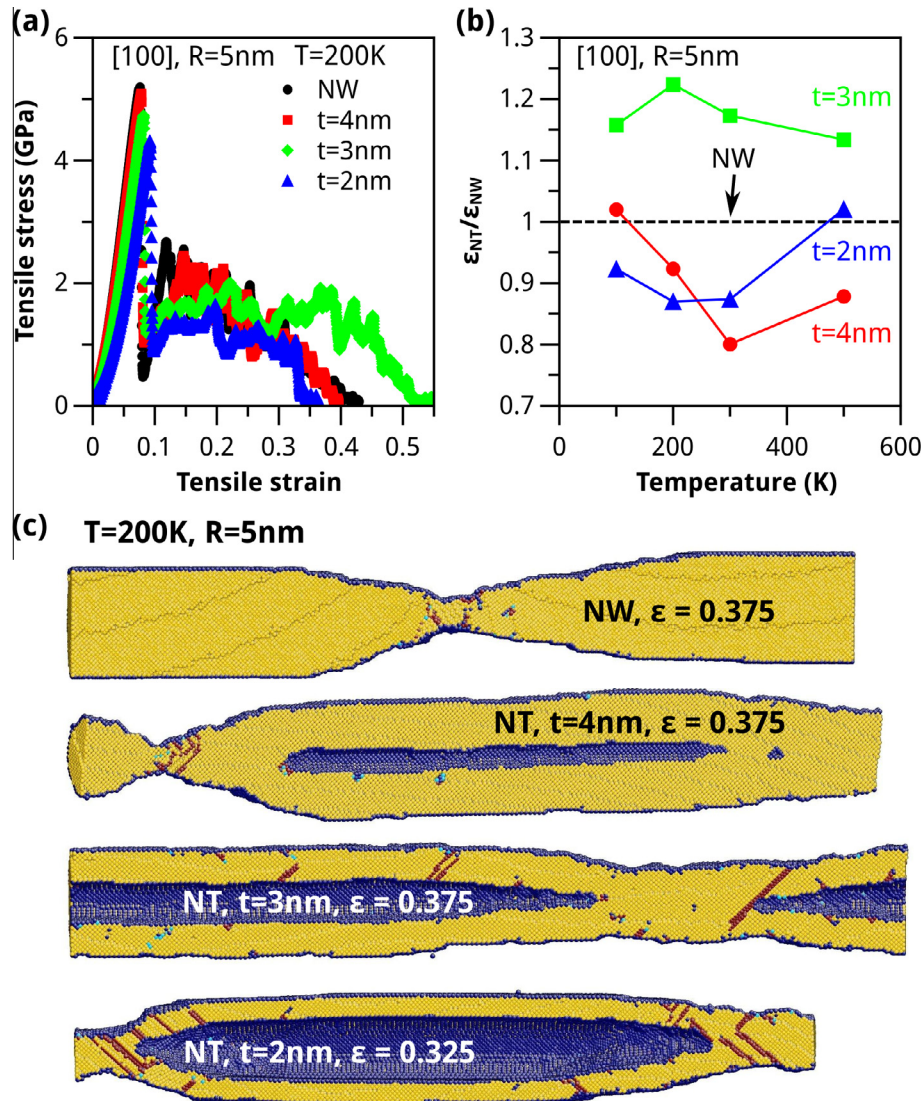


Fig. 9. (a) Tensile stress–strain curves in [100] Au NW and NTs at $T=200$ K. (b) Normalized fracture strain of [100] Au NTs at various temperatures. The dashed black line in (b) indicates the relative fracture strain in the corresponding solid Au NW. (c) The snapshots of the atomistic configurations of each NW and NT during the tensile deformation. The front of each NW or NT was cut to show the interior. The atom colors in (c) correspond to the local lattice structure.

ductility of $\langle 100 \rangle$ Au NTs might be improved as compared to $\langle 100 \rangle$ Au NWs of similar size. The speculation was tested by performing simulations of tensile deformation in $\langle 100 \rangle$ -oriented Au NWs and Au NTs of $R=5$ nm, $t=2$ nm, 3 nm and 4 nm, respectively at temperatures varying from $T=100$ to 500 K up to the fracture point. In those Au NTs no $\langle 100 \rangle$ -to- $\langle 110 \rangle$ reorientation has occurred prior to the tensile deformation. The representative stress–strain curves at $T=200$ K are shown in Fig. 9a, while the normalized fracture strain $\epsilon_{NT}/\epsilon_{NW}$ vs. temperature is plotted in Fig. 9b. Here ϵ_{NT} and ϵ_{NW} represent the fracture strain in Au NTs and the corresponding solid Au NW at the same temperature.

The plots in Fig. 9 show that although the ductility of Au NTs with $R=5$ nm, $t=2$ nm and $t=4$ nm was both lower than the solid NW, the ductility of Au NT with $R=5$ nm and $t=3$ nm was consistently larger than the corresponding solid Au NW at all temperatures, with the maximum improvement of ductility reaching $\sim 25\%$ at

$T=200$ K. The reduced ductility in Au NTs with $t=2$ nm and $t=4$ nm may be attributed to the fact that although the surface stress imposed strong contraction to the Au NT, which made the tensile deformation in Au NT more difficult than in Au NW, the thin wall made the necking more easily. As shown in Fig. 9c, dislocations can easily escape from the free surface in the solid Au NW during the tensile deformation and there was no dislocation pile-up or accumulation in the necking area. However, as the wall thickness in Au NTs decreased, dislocation propagation could be hindered by the inner surface, e.g. in Au NTs with $t=3$ nm and $t=2$ nm, as shown in Fig. 9c, which resulted in dislocation nucleation and pile-up in regions away from the necking area. The influences from the surface stress gradually outweighed those from the thin wall thickness when the ratio of r/R became close to 0.5, which caused the ductility of the Au NT with $R=5$ nm and $t=3$ nm to be particularly large. While it is difficult to rigorously prove if the ratio of $t/R \approx 0.5$ can

lead to optimized ductility in Au NTs, it is supported by additional simulations that the ductility of [110]-oriented Au NTs with $R = 10$ nm, $t = 5$ nm ($t/R = 0.5$) was $\sim 20\%$ larger than the corresponding solid [110] Au NW at 300 K. On the contrary, the ductility of [110]-oriented Au NTs with $R = 10$ nm, $t = 1$ nm, 2 nm and 8 nm were all smaller than the solid Au NW.

It is important to mention that the extraordinary plastic properties in metal NTs predicted in this study can be readily validated by experimental methods [3,53,54] that have been widely used to test metal NWs. For example, recent in situ tensile tests performed by Seo et al. [50,51] have confirmed the CTB-mediated $\langle 100 \rangle / \{100\}$ to $\langle 110 \rangle / \{111\}$ transformation in Au NWs. With the need of little or no adaptation, the state-of-the-art in situ tensile test facilities [50,51] can be used to test the mechanical properties of metal NTs.

5. Conclusions

In summary, we have performed atomistic simulations to investigate the plastic deformation of Au NTs with an emphasis on the surface-stress facilitated structural transformation. Overall, the following conclusions can be made from this work:

- By tuning the wall thickness and axial orientation, Au NTs with ultrahigh strength, plastic flow or ductility can be achieved as compared to the corresponding solid Au NWs of similar size.
- [110]-oriented Au NTs can maintain ultrahigh plastic flow up to 60% tensile strain without sacrificing the yield strength, which may be caused by the formation of a high density of CTBs in those Au NTs prior to the tensile loading due to the strong surface stress.
- [100]-oriented Au NTs experience a phase transformation to [110]-oriented Au NTs when the NT wall thickness is decreased below a threshold. The phase transformation can be induced by the surface stress only and is strongly influenced by temperature.
- There is a universal trend of surface reconstruction to energetically favorable close-packed $\{111\}$ facets in Au NTs regardless of the axial orientation when the NT wall is reduced below certain limit.
- It is expected that this study can stimulate experimental characterization of metal NTs and offer an alternative route to designing superlight, strong, and ductile metallic nanostructures.

Acknowledgments

This research was supported by Fudan University, China, Wuhan Institute of Physics and Mathematics, Chinese Academy of Sciences, China and the University of Manitoba, Canada, and enabled by the use of computing resources provided by West-Grid and Compute/Calcul Canada.

References

- [1] J.R. Greer, J.-Y. Kim, M.J. Burek, The in-situ mechanical testing of nanoscale single-crystalline nanopillars, *JOM* 61 (2009) 19–25.
- [2] J. Wang, F. Sansoz, J. Huang, Y. Liu, S. Sun, Z. Zhang, et al., Near-ideal theoretical strength in gold nanowires containing angstrom scale twins, *Nat. Commun.* 4 (2013) 1742.
- [3] G. Richter, K. Hillerich, D.S. Gianola, R. Monig, O. Kraft, C.A. Volkert, Ultrahigh strength single crystalline nano whiskers grown by physical vapor deposition, *Nano Lett.* 9 (2009) 3048–3052.
- [4] B. Wu, A. Heidelberg, J.J. Boland, J.E. Sader, X. Sun, Y. Li, Microstructure-hardened silver nanowires, *Nano Lett.* 6 (2006) 468–472.
- [5] B. Wu, A. Heidelberg, J.J. Boland, Mechanical properties of ultrahigh-strength gold nanowires, *Nat. Mater.* 4 (2005) 525–529.
- [6] K. Gall, J. Diao, M.L. Dunn, The strength of gold nanowires, *Nano Lett.* 4 (2004) 2431–2436.
- [7] A.T. Jennings, J.R. Greer, Tensile deformation of electroplated copper nanopillars, *Philos. Mag.* 91 (2011) 1108–1120.
- [8] T. Zhu, J. Li, S. Ogata, S. Yip, Mechanics of ultra-strength materials, *MRS Bull.* 34 (2009) 167.
- [9] W. Liang, M. Zhou, Response of copper nanowires in dynamic tensile deformation, *Proc. Inst. Mech. Eng. Part C J. Mech. Eng. Sci.* 218 (2004) 599–606.
- [10] F. Tavazza, L.E. Levine, A.M. Chaka, Elongation and breaking mechanisms of gold nanowires under a wide range of tensile conditions, *J. Appl. Phys.* 106 (2009) 043522–043522-10.
- [11] C. Deng, F. Sansoz, Near-ideal strength in gold nanowires achieved through microstructural design, *ACS Nano.* 3 (2009) 3001–3008.
- [12] M.B. Lowry, D. Kiener, M.M. LeBlanc, C. Chisholm, J.N. Florando, J.W. Morris Jr., et al., Achieving the ideal strength in annealed molybdenum nanopillars, *Acta Mater.* 58 (2010) 5160–5167.
- [13] S. Hao, L. Cui, D. Jiang, X. Han, Y. Ren, J. Jiang, et al., A transforming metal nanocomposite with large elastic strain, low modulus, and high strength, *Science* 339 (2013) 1191–1194.
- [14] Y. Yue, N. Chen, X. Li, S. Zhang, Z. Zhang, M. Chen, et al., Crystalline liquid and rubber-like behavior in Cu nanowires, *Nano Lett.* 13 (2013) 3812–3816.
- [15] Y. Yue, P. Liu, Z. Zhang, X. Han, E. Ma, Approaching the theoretical elastic strain limit in copper nanowires, *Nano Lett.* 11 (2011) 3151–3155.
- [16] B. Peng, M. Locascio, P. Zapol, S. Li, S.L. Mielke, G.C. Schatz, et al., Measurements of near-ultimate strength for multiwalled carbon nanotubes and irradiation-induced cross-linking improvements, *Nat. Nanotechnol.* 3 (2008) 626–631.
- [17] M.-F. Yu, O. Lourie, M.J. Dyer, K. Moloni, T.F. Kelly, R.S. Ruoff, Strength and breaking mechanism of multiwalled carbon nanotubes under tensile load, *Science* 287 (2000) 637–640.
- [18] Y. Sun, B. Mayers, Y. Xia, Metal nanostructures with hollow interiors, *Adv. Mater.* 15 (2003) 641–646.
- [19] H. Cao, L. Wang, Y. Qiu, Q. Wu, G. Wang, L. Zhang, et al., Generation and growth mechanism of metal (Fe, Co, Ni) nanotube arrays, *ChemPhysChem* 7 (2006) 1500–1504.
- [20] M. Wirtz, M. Parker, Y. Kobayashi, C.R. Martin, Template-synthesized nanotubes for chemical separations and analysis, *Chem. Eur. J.* 8 (2002) 3572–3578.
- [21] C. Mu, Y.-X. Yu, R.M. Wang, K. Wu, D.S. Xu, G.-L. Guo, Uniform metal nanotube arrays by multistep template replication and electrodeposition, *Adv. Mater.* 16 (2004) 1550–1553.
- [22] H. Zhu, H. Chen, J. Wang, Q. Li, Fabrication of Au nanotube arrays and their plasmonic properties, *Nanoscale* 5 (2013) 3742–3746.
- [23] H.-W. Wang, C.-F. Shieh, H.-Y. Chen, W.-C. Shiu, B. Russo, G. Cao, Standing [111] gold nanotube to nanorod arrays via template growth, *Nanotechnology* 17 (2006) 2689.
- [24] Y. Sun, B.T. Mayers, Y. Xia, Template-engaged replacement reaction: a one-step approach to the large-scale synthesis of metal nanostructures with hollow interiors, *Nano Lett.* 2 (2002) 481–485.
- [25] Y. Oshima, A. Onga, K. Takayanagi, Helical gold nanotube synthesized at 150 K, *Phys. Rev. Lett.* 91 (2003) 205503.

- [26] M. Davenport, K. Healy, Z.S. Siwy, Ag nanotubes and Ag/AgCl electrodes in nanoporous membranes, *Nanotechnology* 22 (2011) 155301.
- [27] M.J. Lagos, F. Sato, J. Bettini, V. Rodrigues, D.S. Galvão, D. Ugarte, Observation of the smallest metal nanotube with a square cross-section, *Nat. Nanotechnol.* 4 (2009) 149–152.
- [28] P.A.S. Autreto, M.J. Lagos, F. Sato, J. Bettini, A.R. Rocha, V. Rodrigues, et al., Intrinsic stability of the smallest possible silver nanotube, *Phys. Rev. Lett.* 106 (2011) 065501.
- [29] J. Sun, J. Zhang, W. Liu, S. Liu, H. Sun, K. Jiang, et al., Shape-controlled synthesis of silver nanostructures, *Nanotechnology* 16 (2005) 2412.
- [30] M. Venkata Kamalakar, A.K. Raychaudhuri, A novel method of synthesis of dense arrays of aligned single crystalline copper nanotubes using electrodeposition in the presence of a rotating electric field, *Adv. Mater.* 20 (2008) 149–154.
- [31] P. Mohanty, T. Kang, B. Kim, J. Park, Synthesis of single crystalline tellurium nanotubes with triangular and hexagonal cross sections, *J. Phys. Chem. B* 110 (2006) 791–795.
- [32] J.Y. Guo, C.X. Xu, A.M. Hu, K.D. Oakes, F.Y. Sheng, Z.L. Shi, et al., Sintering dynamics and thermal stability of novel configurations of Ag clusters, *J. Phys. Chem. Solids* (2012).
- [33] J.W. Kang, H.J. Hwang, O.-K. Kwon, Atomistic study of double-wall copper nanotubes, *J. Korean Phys. Soc.* 42 (2003) S708–S712.
- [34] W.-S. Su, H.-T. Chen, J.-G. Chang, Y.-T. Wang, W.-J. Lee, Investigation into the formation of 13–6 helical multi-shell gold nanowires, *Comput. Mater. Sci.* 82 (2014) 226–230.
- [35] L. Wang, C. Peng, J. Gong, Molecular dynamics study of the mechanics for Ni single-wall nanowires, *Eur. J. Mech. A Solids* 28 (2009) 877–881.
- [36] J.-F. Su, H.-Y. Song, M.-R. An, Molecular dynamics simulation on mechanical properties of gold nanotubes, *Acta Phys. Sin.* 6 (2013) 018.
- [37] M. Das, P. Mukherjee, S. Konar, B.C. Gupta, Work function and Young's modulus of platinum nanotubes: density functional study, *Phys. Status Solidi B, Basic Solid State Phys.* 250 (2013) 1519–1525.
- [38] E.P.M. Amorim, A.J.R. da Silva, E.Z. da Silva, Computer simulations of copper and gold nanowires and single-wall nanowires, *J. Phys. Chem. C* 112 (2008) 15241–15246.
- [39] J. Zhang, C. Wang, R. Chowdhury, S. Adhikari, Small-scale effect on the mechanical properties of metallic nanotubes, *Appl. Phys. Lett.* 101 (2012) 093109.
- [40] C. Ji, H.S. Park, Geometric effects on the inelastic deformation of metal nanowires, *Appl. Phys. Lett.* 89 (2006) 181916.
- [41] C. Ji, H.S. Park, Characterizing the elasticity of hollow metal nanowires, *Nanotechnology* 18 (2007) 115707.
- [42] M. Sun, F. Xiao, C. Deng, Near-ideal strength in metal nanotubes revealed by atomistic simulations, *Appl. Phys. Lett.* 103 (2013) 231911.
- [43] J. Diao, K. Gall, M.L. Dunn, Surface-stress-induced phase transformation in metal nanowires, *Nat. Mater.* 2 (2003) 656–660.
- [44] H.S. Park, K. Gall, J.A. Zimmerman, Shape memory and pseudoelasticity in metal nanowires, *Phys. Rev. Lett.* 95 (2005) 255504.
- [45] S. Plimpton, Fast parallel algorithms for short-range molecular dynamics, *J. Comput. Phys.* 117 (1995) 1–19.
- [46] G. Grochola, S.P. Russo, I.K. Snook, On fitting a gold embedded atom method potential using the force matching method, *J. Chem. Phys.* 123 (2005) 204719.
- [47] C. Deng, F. Sansoz, Fundamental differences in the plasticity of periodically twinned nanowires in Au, Ag, Al, Cu, Pb and Ni, *Acta Mater.* 57 (2009) 6090–6101.
- [48] C. Deng, F. Sansoz, Enabling ultrahigh plastic flow and work hardening in twinned gold nanowires, *Nano Lett.* 9 (2009) 1517–1522.
- [49] J. Li, AtomEye: an efficient atomistic configuration viewer, *Model. Simul. Mater. Sci. Eng.* 11 (2003) 173.
- [50] J.-H. Seo, Y. Yoo, N.-Y. Park, S.-W. Yoon, H. Lee, S. Han, et al., Superplastic deformation of defect-free Au nanowires via coherent twin propagation, *Nano Lett.* 11 (2011) 3499–3502.
- [51] J.-H. Seo, H.S. Park, Y. Yoo, T.-Y. Seong, J. Li, J.-P. Ahn, et al., Origin of size dependency in coherent-twin-propagation-mediated tensile deformation of noble metal nanowires, *Nano Lett.* 13 (2013) 5112–5116.
- [52] B. Wang, S. Yin, G. Wang, A. Buldum, J. Zhao, Novel structures and properties of gold nanowires, *Phys. Rev. Lett.* 86 (2001) 2046.
- [53] D.S. Gianola, C. Eberl, Micro- and nanoscale tensile testing of materials, *JOM* 61 (2009) 24–35.
- [54] Y. Zhu, H.D. Espinosa, An electromechanical material testing system for in situ electron microscopy and applications, *Proc. Natl. Acad. Sci. U.S.A.* 102 (2005) 14503–14508.